Journal of Materials Chemistry A

PAPER

View Article Online
View Journal | View Issue

Cite this: J. Mater. Chem. A, 2017, 5, 23170

From covalent triazine-based frameworks to N-doped porous carbon/reduced graphene oxide nanosheets: efficient electrocatalysts for oxygen reduction†

Long Jiao,‡[a] Yingli Hu,‡[a] Huanxin Ju,[b] Chunde Wang,[a] Min-Rui Gao,[a] Qing Yang,[a] Junfa Zhu,[b] Shu-Hong Yu[a] and Hai-Long Jiang*[a]

Received 21st August 2017
Accepted 10th October 2017

DOI: 10.1039/c7ta07387a

rsc.li/materials-a

By selecting 4,4′-dicyanobiphenyl (DCBP) as a building block, porous covalent triazine-based frameworks (CTFs) incorporating pyridinic N only have been deliberately fabricated. Upon pyrolysis, the CTF-templated N-doped and hierarchically porous carbons (NHCs) exhibit high surface area, adjustable pore structure and well-controlled doping of pyridinic and graphitic N species. The above CTFs have been rationally grown onto highly conductive reduced graphene oxide (rGO) to afford CTF/rGO hybrids. The subsequent pyrolysis gives sandwich-like NHC/rGO composites, which synergistically integrate respective advantages of both the components of NHC and rGO, thus offering excellent electrocatalytic performance for the oxygen reduction reaction (ORR). Significantly, the resultant NHC/rGO-950 exhibits a more positive onset and half-wave potential, higher diffusion-limited current density and better long-term stability than the state-of-the-art Pt/C and is among the best of previously reported metal-free electrocatalysts, in alkaline solution. Such rGO-templated NHCs based on CTFs offer a promising strategy to design highly efficient metal-free ORR electrocatalysts for fuel cells.

Introduction

With increasing concerns on the global energy crisis, great efforts have been made to develop energy conversion and storage devices including fuel cells and metal–air batteries, in which efficient electrocatalysts for the oxygen reduction reaction (ORR) are crucial to achieve the optimal performance of these devices.[1–13] Currently, Pt and its alloys are the most effective electrocatalysts employed for the ORR, but they suffer from high cost, poor stability, *etc.*[3,4,14–21] Much endeavor has been devoted to the exploration of Pt alternatives including metal oxides or sulfides[22–28] and metal/nitrogen co-doped carbon (M/N–C) materials,[29–32] particularly, the latter of which are very promising in both acidic and alkaline electrolytes. Unfortunately, metal-based catalysts usually suffer from dissolution and agglomeration more or less during the ORR process, leading to deteriorated activity.[4,16,24] In contrast, metal-free porous carbon-based materials are inexpensive, well accessible, corrosion resistant and eco-friendly. The incorporation of nonmetal heteroatoms (*e.g.* N, B, S, *etc.*) has been well demonstrated to greatly improve the ORR performance of carbon materials in alkaline media.[33–42] Recently, much effort has been devoted to modulating the charge density of carbons around heteroatoms to enhance the electrochemical performance.[33–42] In addition to tailoring the electronic structure, the exposure of active sites through the fabrication of porous nanostructure and enhancement of electronic conductivity can further improve the ORR performance.[43]

To dope carbon-based materials, nitrogen is an ideal candidate with its slightly smaller atomic radius to carbon but much larger electronegativity. Nitrogen induces charge delocalization of carbon and results in non-electroneutrality of the catalysts, which are recognized as crucial factors for the enhancement of oxygen adsorption and reduction.[36,44–49] The precise control of nitrogen configurations is of prime importance for doping. It has been demonstrated that both pyridinic and graphitic N species are effective in promoting the ORR but pyrrolic N species is not.[45–47] The ORR performance of carbon-based catalysts is also significantly affected by the surface area and porosity, which govern the exposure of active sites and mass transfer efficiency.[30,37] In addition, the electric conductivity, regulated by the degree of sp^2 bonding of carbon

[a]Hefei National Laboratory for Physical Sciences at the Microscale, CAS Key Laboratory of Soft Matter Chemistry, Collaborative Innovation Center of Suzhou Nano Science and Technology, Department of Chemistry, University of Science and Technology of China, Hefei, Anhui 230026, P. R. China. E-mail: jianglab@ustc.edu.cn

[b]National Synchrotron Radiation Laboratory, University of Science and Technology of China, Hefei, Anhui 230029, P. R. China

† Electronic supplementary information (ESI) available: Figures and tables referred in the text and comparison of the literature catalytic parameters of various metal-free electrocatalysts. See DOI: 10.1039/c7ta07387a

‡ These authors contributed equally to this work.

materials, is essential for electron transfer in electrocatalysts.[24,50,51] The introduction of foreign nitrogen sources into carbon precursors often fails in the control of active N species and the pore structure,[52–55] and the generation of the desired configuration of N sites in the resultant carbon materials is extremely challenging.[18]

We decided to tackle the above-mentioned challenges by constructing N-doped porous carbon ORR electrocatalysts with dominant pyridinic and graphitic N incorporation *via* a single porous precursor, covalent triazine-based frameworks (CTFs). CTFs feature tunable N doping and predictable 2D porous structures through a trimerization reaction by selecting appropriate aromatic nitriles as monomers, and they can be further interconnected to afford 3D porous networks with tunable pore structures.[56–63] The designable structure of porous CTFs involving pyridinic N only makes them ideal precursors to afford N-doped porous carbons with inherited active N species and the optimized structure for the ORR. However, the electrical conductivity of CTFs and their derived carbon materials are commonly unsatisfactory due to the low degree of graphitization, which significantly limits the electrochemical application of CTF-based materials.[64,65] Reduced graphene oxide (rGO), which can be obtained from the reduction of graphene oxide (GO), possesses a two-dimensional (2D) sheet-like structure with superior electrical conductivity and excellent chemical stability.[23,66–69] The unique 2D structure, high conductivity and oxygen-enriched groups on the surface make rGO a promising candidate to serve as a suitable template and conductive substrate to induce the oriented growth of CTF-based materials, enhancing their electrochemical performance. For example, Su *et al.* have combined graphene and porous polyaryltriazine-derived frameworks into a high-performance cathode for lithium-ion batteries.[69] Therefore, it is highly desirable and would be feasible to develop an effective method to couple CTF-based materials with rGO that permits synergistically enhanced ORR performance.

In this work, by choosing 4,4′-dicyanobiphenyl (DCBP) as a building block and polyacrylonitrile decorated rGO (PAN/rGO) as a template, hierarchically porous CTFs were readily grown on both sides of PAN/rGO nanosheets to afford sandwich-type CTF/rGO composites, *via* an *in situ* "bottom-up" trimerization of DCBP. Following facile pyrolysis under an N_2 atmosphere, the CTF/rGO composites were further converted to N-doped and hierarchically porous carbon/rGO (denoted as NHC/rGO-*T*; *T* represents pyrolysis temperature) composites (Scheme 1). The abundant pyridinic N atoms in the CTF precursor result in only active pyridinic and graphitic N sites in NHC/rGO-*T*. Moreover, our NHC/rGO-*T* features a high surface area and optimized hierarchically porous structure, which are beneficial to the exposure of active sites and fast diffusion of electrolytes and O_2. Meanwhile, the close contact between NHC and rGO in NHC/rGO-*T* leads to a consecutive conductive network, which is of great importance for electron transfer, and the rGO-induced thin layered structure further shortens the diffusion distance. We believe that the above characteristics synergistically contribute to the enhancement of ORR activity. Remarkably, the resultant NHC/rGO-950 composite exhibits higher ORR performance than the commercial benchmark Pt/C catalyst in 0.1 M KOH solution, including catalytic activity, long-term stability and methanol tolerance.

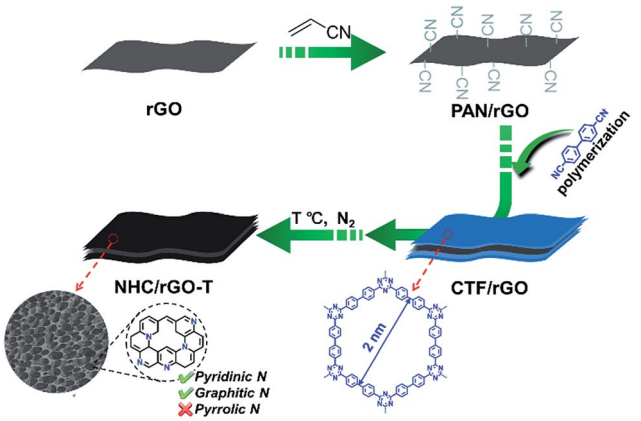

Scheme 1 Illustration of rational stepwise fabrication of the sandwich-like NHC/rGO-*T* layered composite.

Experimental

Materials

All chemicals were purchased from commercial sources and used without further treatment: zinc chloride ($ZnCl_2$, Sinopharm Chemical Reagent Co., Ltd., 98%), 4,4′-dicyanobiphenyl (DCBP, Jinan Henghua Sci. & Tec. Co., Ltd., 99%), graphene oxide (GO, XF Nano, 99.5%), hydrazine hydrate ($N_2H_4 \cdot xH_2O$, Sinopharm Chemical Reagent Co., Ltd., 85%), sodium dodecyl sulfate (SDS, Sinopharm Chemical Reagent Co., Ltd., 86%), sodium (Na, Sinopharm Chemical Reagent Co., Ltd., 99.5%), anhydrous tetrahydrofuran (THF, Sinopharm Chemical Reagent Co., Ltd., 99.5%, anhydrous), acrylonitrile (AN, Chem Greatwall, 99%), pyrrole (py, Aladdin Industrial Corporation, 99%), ammonium persulfate ($(NH_4)_2S_2O_8$, Sinopharm Chemical Reagent Co., Ltd., 98%), ethanol (CH_3CH_2OH, Sinopharm Chemical Reagent Co., Ltd., 99.7%), methanol (CH_3OH, Sinopharm Chemical Reagent Co., Ltd., 99.5%), hydrogen chloride (HCl, Sinopharm Chemical Reagent Co., Ltd., 37%), and potassium hydroxide (KOH, Sinopharm Chemical Reagent Co., Ltd., 85%). De-ionized water with the specific resistance of 18.25 MΩ cm was obtained by reverse osmosis followed by ion-exchange and filtration (Cleaned Water Treatment Co., Ltd., Hefei).

Synthesis of rGO

Graphene oxide (GO, 250 mg) was added into a 250 mL round bottom flask with H_2O (125 mL) and subjected to ultrasonic treatment for 2 h. Then, sodium dodecyl sulfate (1.0 g) and hydrazine hydrate (3 mL) were added into the above GO dispersion and reacted at 80 °C for 12 h with stirring. After the reduction reaction, the mixture was treated by freeze-drying. The freeze-dried solid was subsequently filtered and washed with water and ethanol several times. Finally, the sample was dried at 60 °C in a vacuum to give the rGO.

Synthesis of PAN/rGO

rGO (80 mg) and sodium (0.05 g) were subjected to ultrasonic treatment in anhydrous tetrahydrofuran (THF, 10 mL), thus forming rGO polyanion salts (rGONa). Acrylonitrile (0.64 mL) was added, followed by the reaction at room temperature for 12 h. Polymerization took place on the graphene surfaces, resulting in an intimately mixed composite system. The polymerization was terminated by adding methanol. The black precipitate was centrifuged several times with THF followed by vacuum drying at 60 °C overnight to obtain PAN/rGO as a black powder.

Synthesis of pure CTFs and CTF/rGO composites

In a typical experiment, DCBP monomers (200 mg) and a certain amount of $ZnCl_2$ (1.4 g, 2.0 g or 2.6 g) were mixed together and transferred into a quartz tube under an inert atmosphere. The quartz tube was then evacuated, sealed, and heated to 700 °C for 24 h in the muffle furnace (it took 5 h to reach 700 °C from RT). After the quartz tube was cooled down to room temperature and opened, the resulting CTFs were obtained after washing several times with 1 M HCl. Then, the samples were activated by refluxing in 1 M HCl and ethanol, respectively, for 24 h. The CTF/rGO was synthesized *via* the same procedure except for the addition of PAN/rGO (20 mg) and a fixed amount of $ZnCl_2$ (2.0 g).

Synthesis of NHC/rGO-*T* and pure NHC-950

Typically, 20 mg of activated sample (CTF/rGO) was loaded into a tube furnace and subsequently heated under an N_2 atmosphere. The sample was thermally treated at a heating rate of 5 °C min^{-1} up to 850, 950 or 1050 °C and held at this temperature for 2 hours. Thereafter, it was cooled down to room temperature to yield the final product. NHC-950 was obtained following a similar procedure by replacing NHC/rGO-950 with CTF-10.

Synthesis of pyrrolic-N-NHC/rGO-950

Polypyrrole (Ppy) was firstly synthesized. In brief, a pyrrole (py) monomer (1 mL) was dissolved in a mixture of ethanol (50 mL) and water (50 mL) at 0–5 °C. 0.7 M $(NH_4)_2S_2O_8$ aqueous solution (20 mL) was then added dropwise into the above py solution and stirred for 24 h. Ppy was finally obtained by filtration. Then, the DCBP monomer (100 mg), Ppy (67 mg) and $ZnCl_2$ (2.0 g) were mixed together and transferred into a quartz tube under an inert atmosphere. The latter heat treatment processes are similar to the synthesis of NHC/rGO-950.

Electrochemical measurements

Electrochemical measurements were performed with a CHI 760E electrochemical analyzer (CH Instruments, Inc., Shanghai) and a rotating disk electrode (RDE) (Pine Instruments, Grove city, PA). All electrochemical measurements were conducted in a typical three-electrode setup with a graphite rod counter electrode and Hg/HgO reference electrode. LSV measurements were conducted with a scan rate of 5 mV s^{-1}. Rotating ring-disk electrode (RRDE) measurements were carried out to determine the four-electron selectivity. The disk electrode was scanned at a rate of 10 mV s^{-1}, and the ring electrode potential was set to 1.2 V *vs.* the RHE. All data are presented without iR compensation.

The catalyst ink was prepared by dispersing 2 mg of catalyst into 1 mL of ethanol containing 10 μL of 5 wt% Nafion and sonicated for 30 min. Then, 28 μL of the catalyst ink was loaded onto a GCE of 5 mm diameter (loading amount: ~0.28 mg cm^{-2}). For comparison, Pt/C (20 wt% platinum) was investigated using the same electrochemical tests with a catalyst loading of 0.1 mg cm^{-2}.

The mass activity J_m is derived from the equation:

$$J_m = J_k/m_{cat}$$

where J_k is the kinetic current at 0.8 V and m_{cat} represents the mass of the catalyst. m_{cat} represents the total amount of catalysts for all prepared samples. It is hard to calculate the real active sites/composition because there is still no reliable technique to evaluate the accurate amount of sites in an N-doped carbon system. Therefore, we calculated the mass activity of the catalyst loaded onto the GCE, replacing the mass activity of active sites in catalysts.

Rotating ring-disk electrode (RRDE) measurements were carried out to determine the four-electron selectivity. The disk electrode was scanned at a rate of 10 mV s^{-1}, and the ring electrode potential was set to 1.2 V *vs.* the RHE.

The Nyquist plots of the catalysts were all obtained by applying a sine wave with an amplitude of 5.0 mV over the frequency range 100 kHz to 0.01 Hz at an overpotential of 0.5 V in an O_2 atmosphere.

Characterization

Powder X-ray diffraction (PXRD) patterns were collected on a Japan Rigaku SmartLab™ rotation anode X-ray diffractometer equipped with graphite monochromatized Cu Kα radiation (λ = 1.54 Å). The transmission electron microscopy (TEM) and high-resolution TEM images were acquired on a JEM-2010, and elemental mapping was performed on a JEOL ARM-200F with an electron acceleration energy of 200 kV. Field-emission scanning electron microscopy (FE-SEM) was carried out with a field emission scanning electron microanalyzer (Zeiss Supra 40 scanning electron microscope at an acceleration voltage of 5 kV). The nitrogen sorption measurement was conducted using a Micromeritics ASAP 2020 system at 77 K. Prior to the nitrogen adsorption/desorption measurement, the samples were dried overnight at 160 °C under vacuum. X-ray photoelectron spectroscopy (XPS) measurements were performed by using an ESCALAB 250 high-performance electron spectrometer using monochromatized Al Kα ($h\nu$ = 1486.7 eV) as the excitation source and at the Catalysis and Surface Science Endstation at the BL11U beamline in the National Synchrotron Radiation Laboratory (NSRL) in Hefei, China. The core level spectra of N 1s were recorded with a VG SCIENTA R4000 electron energy analyzer and using a monochromatic Al Kα X-ray source ($h\nu$ = 1486.7 eV) at normal incidence. The binding energy was

calibrated using the C 1s from graphene oxide nanosheets located at 284.8 eV as the reference. The spectral decomposition was performed using the XPS Peak 41 program with Gaussian functions after subtraction of a Shirley background.

Raman scattering spectra were recorded with a Renishaw System 2000 spectrometer using the 514.5 nm line of Ar^+ for excitation. Fourier transform infrared (FT-IR) spectra were measured using a Nicolet 8700 FTIR E.S.D. and KBr pellet samples. The sample for the FT-IR test was obtained by stopping the trimerization process of DCBP at 450 °C. Elemental analysis (EA) was performed on a VarioELIII analyzer. Nitrogen K-edge near-edge X-ray absorption fine structure (NEXAFS) spectroscopy was performed on a Soft X-ray Magnetic Circular Dichroism Endstation (SXMCD) in total electron yield (TEY) mode at NSRL. The NEXAFS spectra were analyzed by least-squares fitting using the WinXAS 3.1 program, and the peak fitting procedure was accomplished with Gaussian functions in conjunction with an arctan function background subtraction.

Results and discussion

To obtain relatively large pore sizes/volumes that are required for efficient electrolyte transfer and O_2 diffusion, DCBP, a monomer with a molecular length of 1.3 nm, has been deliberately employed to undergo trimerization to give 2D sheets with 2 nm micropores (Scheme 1), which are subsequently self-organized and cross-linked into porous 3D networks with high surface areas. The pore structure can be well tuned by changing the mass ratio of DCBP and $ZnCl_2$, of which the optimized mass ratio (1 : 10) of DCBP : $ZnCl_2$ gives the product CTF-10 with maximal pore volume, optimal pore structure and a very high surface area among all CTFs (Fig. S1†). Starting from free-standing sheets of PAN/rGO (Fig. 1a and S2†), the CTF/rGO composite based on an optimized mass ratio (DCBP : $ZnCl_2$ = 1 : 10) has been fabricated with a sandwich-like layered structure, in which both sides of rGO sheets are covered by porous CTFs (Fig. 1b and S3†). This is, as far as we know, the first rational assembly of the CTF/rGO sheet-like composite based on the rGO template for electrocatalysis.

The CTF/rGO then underwent pyrolysis at different temperatures under an N_2 atmosphere to produce NHC/rGO-*T* (*T* = 850, 950, and 1050 °C). The optimal pyrolysis temperature was determined to be 950 °C, and the resultant NHC/rGO-950 inherits a sheet-like morphology with sharp and well-defined edges *via* the induction effect of the 2D rGO template. The scanning electron microscopy (SEM) image shows that the porous NHC is distributed on both sides of rGO homogeneously. Despite possessing a similar high BET surface area, the sheet-like morphology of NHC/rGO-950 is quite different from the irregular bulk NHC-950 directly obtained from CTF-10 in the absence of rGO (Fig. 1c, S4 and S5†). The transmission electron microscopy (TEM) image clearly shows the existence of mesopores with a size of ~5 nm (Fig. 1d, indicated by dashed yellow circles), which might be inherited from the mesopores of the CTF/rGO composite. Owing to the high porosity of CTF/rGO, the BET surface area of NHC/rGO-950 reached 1344 $m^2\ g^{-1}$ with a hierarchical pore size extending to ~80 nm (peak: ~50 nm),

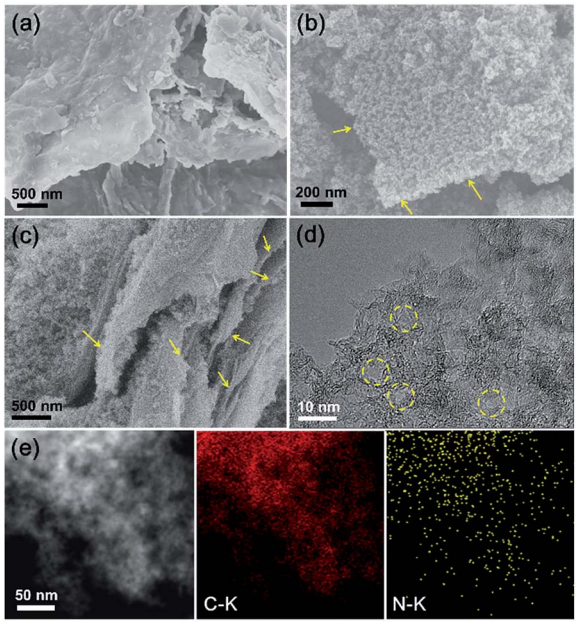

Fig. 1 SEM images of (a) PAN/rGO, (b) CTF/rGO and (c) NHC/rGO-950. (d) TEM image and (e) HADDF-STEM image and C and N elemental mapping images of NHC/rGO-950. The yellow arrows indicate the GO layers and the dashed yellow circles highlight the pores involved in the structure.

which is similar to those of NHC/rGO-850 and NHC/rGO-1050, revealing the good inheritance of the pore structure from CTF/rGO (Fig. 2). The significant pore size distribution in the range of 4–10 nm for NHC/rGO-950 agrees well with the TEM observation mentioned above (Fig. S6†). The high-angle annular dark-field scanning transmission electron microscopy (HADDF-STEM) and elemental mapping images show the uniform nitrogen distribution throughout the carbon matrix, demonstrating the advantage of CTFs in the controllable and homogeneous N doping (Fig. 1e).

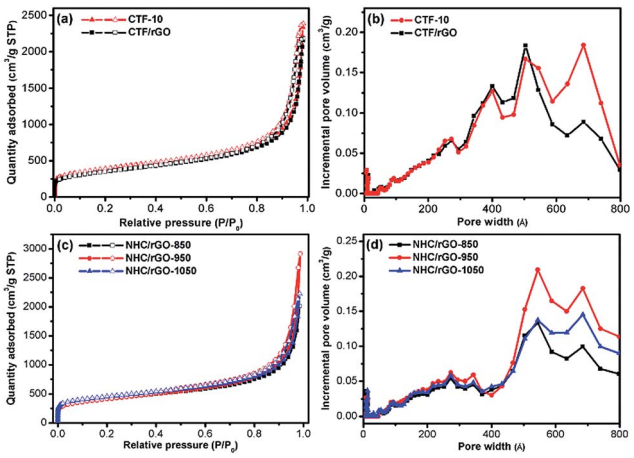

Fig. 2 (a) N_2 sorption isotherms of CTF-10 and CTF/rGO at 77 K and (b) their corresponding pore size distributions calculated by the DFT model. (c) N_2 sorption isotherms of NHC/rGO-*T* at 77 K and (d) the corresponding pore size distributions calculated by using the DFT model.

The X-ray photoelectron spectroscopy (XPS) study was conducted to probe the chemical compositions and the configurations of N species in NHC/rGO-950. As shown in Fig. S7,† the XPS spectrum demonstrates the existence of C, N and O. The high-resolution N 1s spectrum can be mainly fitted into two peaks, corresponding to pyridinic N and graphitic N (Fig. 3a). It is interesting that no pyrrolic N was detected, while it is present in most other reported N-doped carbon materials.[70–73] Similar results can also be obtained for NHC/rGO-850 and NHC/rGO-1050, as well as NHC-950 directly pyrolyzed from pure CTF-10 (Fig. 3a, S8 and S9†). This phenomenon is attributed to the exclusive existence of pyridinic nitrogen in the structure of CTFs, which can be transformed into pyridinic and graphitic nitrogens but not pyrrolic nitrogen during the pyrolysis. The very small oxidized-N peak in NHC/rGO-950 might come from reduced graphene oxide. To glean further experimental evidence on N configurations, N K-edge near-edge X-ray absorption fine structure (NEXAFS) spectroscopy, which is chemical state sensitive, was employed to investigate NHC/rGO-950 (Fig. 3b). There are two π^* peaks at 398.5 and 402 eV, corresponding to pyridinic N and graphitic N, respectively.[22] The peak at 399.4 eV suggests a well-defined structure of C=N.[74] The broaden peak centered at 406 eV is the general transition from the N 1s core level to the C–N σ^* state.[22,55] Obviously, no pyrrolic N signal (~400 eV) is detectable.[74] This result is fully consistent with the above XPS results and further confirms the presence of pyridinic N and graphitic N, but not pyrrolic N species. It has been generally accepted that only pyridinic N and graphitic N can behave as active sites for ORR catalysis. Pyridinic N atoms can bind with and activate oxygen molecules, and graphitic N can promote the electron transfer and facilitate the oxygen dissolution on its adjacent carbon atoms.[75–78] The absence of inactive pyrrolic N species in NHC/rGO-950 highlights the advantage of pyridinic N enriched CTFs as precursors in the controlled doping of highly active N sites in the carbon materials, which is significant to enhance ORR activity.

The powder X-ray diffraction (PXRD) pattern of NHC/rGO-950 as well as NHC shows two prominent diffraction peaks at 26.0° and 43.7°, corresponding to the (002) and (101) reflections of graphitized carbon, respectively (Fig. 3c). The existence of these two diffraction peaks suggests a relatively high graphitization degree of NHC/rGO-950 and NHC, which has been further characterized by the Raman spectra. The D and G bands at 1332 and 1584 cm^{-1} correspond to the disordered and sp^2 hybridized graphitic carbon, respectively, and the intensity ratio of I_D/I_G is determined by the graphitization degree of carbon. The I_D/I_G values of NHC/rGO-950 and NHC-950 are 1.02 and 1.05, respectively, supporting the PXRD results and suggesting their good graphitization (Fig. 3c and d).

Encouraged by the above results, the electrocatalytic ORR performance of the NHC/rGO catalysts was evaluated. To this end, thin films were prepared on glassy carbon electrodes for cyclic voltammetry (CV) in O_2-saturated 0.1 M KOH in a home-made polytetrafluoroethylene (PTFE) electrochemical cell. As shown in Fig. 4a, no obvious redox peak is observed for NHC/rGO-950 in N_2-saturated electrolyte; in contrast, when the solution is saturated with O_2, a well-defined cathodic peak clearly appears at 0.80 V, highlighting its electrocatalytic ORR activity comparable to that of the benchmark Pt/C catalyst (Fig. S10†). The linear scanning voltammetry (LSV) curves

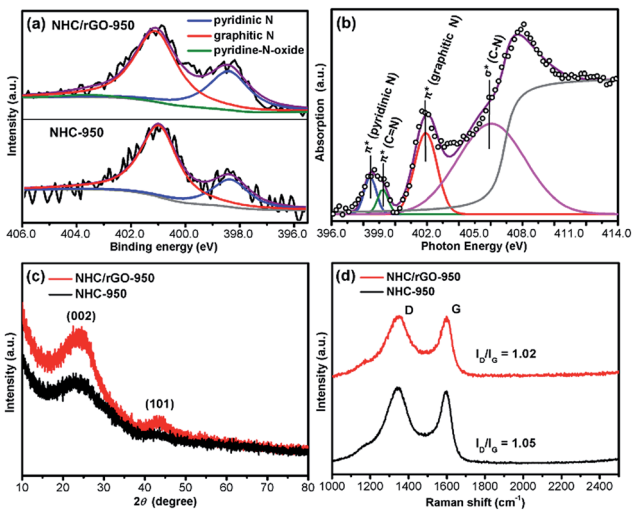

Fig. 3 (a) The high-resolution N 1s XPS spectra of NHC/rGO-950 and NHC-950 (pyrrolic N: 399.5 eV). (b) N K-edge NEXAFS spectrum of NHC/rGO-950 (pyrrolic N: ~400 eV). (c) Powder XRD patterns and (d) Raman scattering spectra of NHC/rGO-950 and NHC-950.

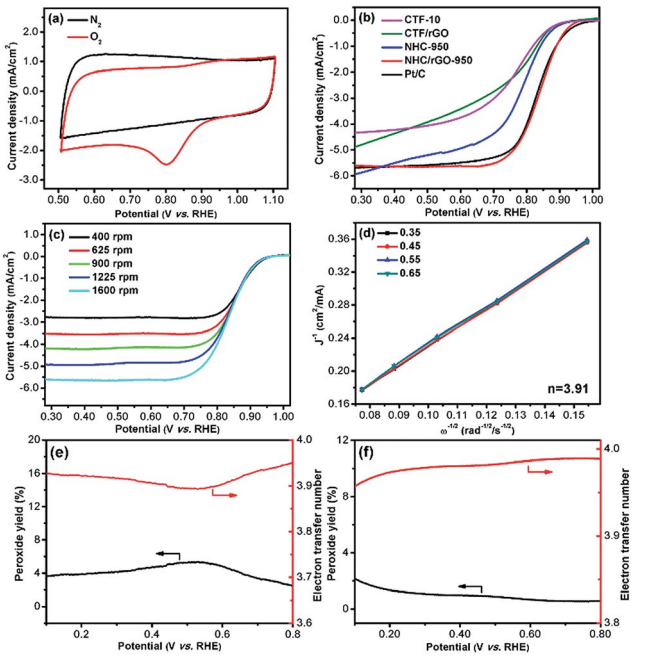

Fig. 4 Electrochemical ORR performance of NHC/rGO-950. (a) CV in N_2 and O_2-saturated 0.1 M KOH solution at a scan rate of 100 mV s^{-1}, (b) LSV in O_2-saturated 0.1 M KOH solution at a rotation speed of 1600 rpm, (c) LSV at different RDE rotation rates in O_2-saturated 0.1 M KOH solution, (d) K–L plots and electron transfer numbers at different potentials. A peroxide yield with regard to the total oxygen reduction products and the calculated electron transfer number of (e) NHC/rGO-950 and (f) Pt/C in O_2-saturated 0.1 M KOH.

collected on a rotating disk electrode (RDE) after the elimination of capacitive currents show that NHC/rGO-950 possesses a prominent catalytic activity with an onset potential of 0.95 V, a half-wave potential of 0.83 V and a diffusion-limited current density of -5.64 mA cm^{-2} (Fig. 4b), which are better than that of commercial Pt/C. In addition, CTF-10, CTF/rGO, NHC-950 and CTF/rGO-T ($T = 850, 950, 1050$) were also carefully examined for comparison. As expected, NHC/rGO-950 showed the highest activity among the studied catalysts (Fig. 4b and S11†). Through pore size distribution analysis, elemental analysis, and electrochemical impedance spectroscopy (EIS), the essential influences by both pyrolysis temperature and rGO introduction on the ORR performance are manifested. All NHC/rGO-T composites show a similar surface area, while NHC/rGO-950 presents the largest pore volume, most of which is ascribed to the pores with sizes beyond 40 nm that are favorable for mass transfer (Fig. 2c and d). The content of N species, especially the most active pyridinic N, in NHC/rGO-950 is comparable to that in NHC/rGO-850 but larger than that in NHC/rGO-1050, which accounts for the inferior performance of the latter (Fig. S12 and Table S1†). Meanwhile, compared to pure NHC-950, NHC/rGO-950 possesses similar N contents but a smaller radius in the Nyquist plot, reflecting the higher conductivity of NHC/rGO-950, which results in its much better ORR activity, and this also explains the inferior performance of CTF materials (Fig. 4b, S13, S14 and Table S1†). Furthermore, the rGO-induced 2D lamellar structure of NHC/rGO-950 nanosheets makes them more favorable to conduct mass transfer than the bulk NHC-950 (Fig. 1c and S4†). The combination of the above characteristics make NHC/rGO-950 the best ORR catalyst in our investigation. In addition, to further clarify the effect of pyrrolic N, pyrrolic-N-containing NHC/rGO-950 (pyrrolic-N-NHC/rGO-950), with similar N contents, pore size distribution and conductivity to NHC/rGO-950, has also been prepared (Fig. S15–S17†). The inferior performance of pyrrolic-N-NHC/rGO-950 to NHC/rGO-950 clearly exhibits that the absence of pyrrolic N in NHC/rGO-950 plays a significant role in the enhancement of ORR activity (Fig. S18†).

To gain more insight into the reaction kinetics of NHC/rGO-950, LSV curves were measured under different rotating speeds from 400 to 1600 rpm, showing a well-defined platform of diffusion-limited current density (Fig. 4c). The electron transfer number (n) calculated from the LSV curves according to the Koutecky–Levich (K–L) equation was determined to be 3.91, suggesting an ideal four-electron pathway of NHC/rGO-950 for the ORR (Fig. 4d). The rotating ring-disk electrode (RRDE) test was adopted to further demonstrate the high selectivity of the NHC/rGO-950 toward the four-electron reduction of oxygen with a low H_2O_2 yield at about 4%, which is comparable to that of Pt/C (Fig. 4e and f). In addition, the kinetic current density and mass activity for NHC/rGO-950 at 0.8 V are 14.5 mA cm^{-2} and 51.6 mA mg_{cat}^{-1}, respectively, demonstrating a better kinetic behavior of NHC/rGO-950 than most of the reported carbon-based catalysts but inferior to Pt-based catalysts (Table S2†). Moreover, the excellent ORR activity of NHC/rGO-950 can be further supported by the faster current growth along with the increase of overpotential and the smaller Tafel slope (74 mV per decade) than Pt/C (80 mV per decade), illustrating the more favorable ORR kinetics of the former (Fig. S19†). Our studies suggest that NHC/rGO-950 is among the best of all reported metal-free carbon-based ORR catalysts (Fig. 5 and Table S2†). In view of the excellent ORR in alkaline solution, the ORR activity of NHC/rGO-950 in 0.1 M $HClO_4$ has also been tested. However, it presents low ORR activity due to the protonation of the surface N-groups under acidic conditions, which is consistent with most reported results on N-doped carbon (Fig. S20†).[93]

In addition to high ORR activity, excellent stability and methanol tolerance are also required for electrocatalysts to be practically useful for fuel cells. We evaluated the stability of NHC/rGO-950 at a constant voltage of 0.8 V for 20 000 seconds in O_2-saturated 0.1 M KOH solution. 97% of the current density remained, which is higher than that of the commercial Pt/C (95%) (Fig. 6a). To exclude the possibility of ORR activities induced by any possible metal contaminants, inductively coupled plasma-mass spectrometry (ICP-MS) analysis was conducted on NHC/rGO-950 before and after long-term electrocatalytic tests. The results show that negligible metal (Fe, Co, Pt, Zn) contamination ($\leq$20 ppm) is present in the final products (Table S3†), revealing that N heteroatoms are responsible for ORR catalysis.[94] The washed electrode after a long-term measurement was subjected to an electrocatalytic test in a fresh portion of 0.1 M KOH (Fig. S21†). The activity improvement in fresh electrolyte was not observed, revealing that the above slight deterioration in performance might not be due to the contamination. Furthermore, the reproducibility tests for 3 different samples of NHC/rGO-950 on LSV and stability have also been investigated, and the results clearly

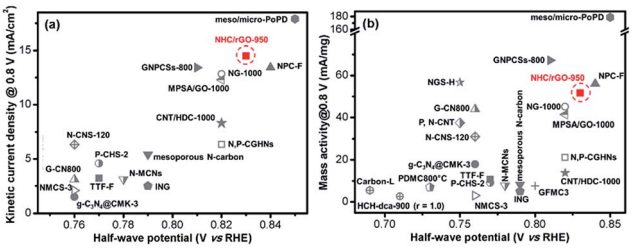

Fig. 5 Comparison of ORR performance of NHC/rGO-950 with other metal-free electrocatalysts previously reported in 0.1 M KOH solution based on (a) a kinetic current density at 0.8 V *vs.* the half-wave potential and (b) a mass activity (calculated by the total mass loading of the catalysts) at 0.8 V *vs.* the half-wave potential.[16,20,40–42,50,54,75,79–92]

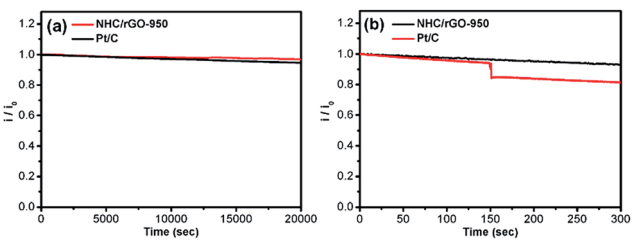

Fig. 6 (a) Time-dependent current density curves and (b) methanol-tolerance evaluation of NHC/rGO-950 in 0.1 M KOH solution.

show the reliable performance of the optimal NHC/rGO-950 catalyst (Fig. S22†). Moreover, the methanol crossover effect should be considered given that methanol in the anode can sometimes permeate through the polymer membrane to the cathode and seriously lowers the ORR performance of cathode catalysts in direct methanol fuel cells. Therefore, the tolerance of NHC/rGO-950 against methanol poisoning was studied. After the addition of 3 M methanol, almost no noticeable current variation was observed for NHC/rGO-950, which is in stark contrast to the significant decline of Pt/C activity (Fig. 6b). These results unambiguously suggest higher stability, greater durability and much better tolerance to the methanol crossover effect of NHC/rGO-950 than those of Pt/C.

Conclusions

In summary, following a rGO-templated DCBP self-polymerization process, we have rationally constructed a sandwich-like pyridinic N-enriched CTF/rGO hybrid, which subsequently affords a sheet-like NHC/rGO-950 composite with dominant pyridinic and graphitic N incorporation, as a highly efficient ORR catalyst. Based on the judiciously selected porous CTF precursor, active N species can be conveniently controlled in the resultant carbon materials. This is a significant improvement to other traditional ways of introducing N species in which the control of N configurations is difficult. Thanks to the synergistic effect between CTF-derived NHC and 2D rGO in terms of high surface area, hierarchical pores, controllable incorporation of active N species, favorable mass transfer and high conductivity, the layered NHC/rGO-950 exhibits superb ORR activity and ultrahigh stability as well as excellent methanol tolerance. To the best of our knowledge, the overall catalytic performance of NHC/rGO-950 surpasses the state-of-the-art Pt/C and almost all metal-free catalysts in alkaline solution reported so far. The inexpensive raw materials and facile preparation as well as the outstanding electrocatalytic performance make NHC/rGO-950 a very promising ORR catalyst in fuel cells. The adjustable size and large diversity of CTF monomers could enable desirable element doping and controllable pore structure in the resultant CTFs; the strategy presented here holds great promise for the fabrication of high-performance metal-free electrocatalysts, on the basis of versatile CTF/rGO composites by integrating their respective merits.

Conflicts of interest

There are no conflicts to declare.

Acknowledgements

We are grateful to Dr Zhiyong U. Wang at Troy University (USA) for helpful discussions and manuscript refinement. This work is supported by the NSFC (21371162, 21673213, and 21521001), the National Research Fund for Fundamental Key Project (2014CB931803) and the Recruitment Program of Global Youth Experts.

Notes and references

1 B. C. H. Steele and A. Heinzel, *Nature*, 2001, **414**, 345–352.
2 M. Winter and R. J. Brodd, *Chem. Rev.*, 2004, **104**, 4245–4270.
3 R. Bashyam and P. Zelenay, *Nature*, 2006, **443**, 63–66.
4 Y.-J. Wang, D. P. Wilkinson and J. Zhang, *Chem. Rev.*, 2011, **111**, 7625–7651.
5 Y. Nie, L. Li and Z. Wei, *Chem. Soc. Rev.*, 2015, **44**, 2168–2201.
6 L. Dai, Y. Xue, L. Qu, H.-J. Choi and J.-B. Baek, *Chem. Rev.*, 2015, **115**, 4823–4892.
7 W. He, Y. Wang, C. Jiang and L. Lu, *Chem. Soc. Rev.*, 2016, **45**, 2396–2409.
8 M. Shao, Q. Chang, J.-P. Dodelet and R. Chenitz, *Chem. Rev.*, 2016, **116**, 3594–3657.
9 M. Zhou, H.-L. Wang and S. Guo, *Chem. Soc. Rev.*, 2016, **45**, 1273–1307.
10 J. Du, J. Qi, D. Wang and Z. Tang, *Energy Environ. Sci.*, 2012, **5**, 6914–6918.
11 H. Tang, H. Yin, J. Wang, N. Yang, D. Wang and Z. Tang, *Angew. Chem., Int. Ed.*, 2013, **52**, 5585–5589.
12 H. Yin, S. Zhao, K. Zhao, A. Muqsit, H. Tang, L. Chang, H. Zhao, Y. Gao and Z. Tang, *Nat. Commun.*, 2015, **6**, 6430.
13 S. Zhao, Y. Wang, J. Dong, C.-T. He, H. Yin, P. An, K. Zhao, X. Zhang, C. Gao, L. Zhang, J. Lv, J. Wang, J. Zhang, A. M. Khattak, N. A. Khan, Z. Wei, J. Zhang, S. Liu, H. Zhao and Z. Tang, *Nat. Energy*, 2016, **1**, 16184.
14 A. Morozan, B. Jousselme and S. Palacin, *Energy Environ. Sci.*, 2011, **4**, 1238–1254.
15 I. E. L. Stephens, A. S. Bondarenko, U. Grønbjerg, J. Rossmeisl and I. Chorkendorff, *Energy Environ. Sci.*, 2012, **5**, 6744–6762.
16 R. Silva, D. Voiry, M. Chhowalla and T. Asefa, *J. Am. Chem. Soc.*, 2013, **135**, 7823–7826.
17 X. Huang, Z. Zhao, L. Cao, Y. Chen, E. Zhu, Z. Lin, M. Li, A. Yan, A. Zettl, Y. M. Wang, X. Duan, T. Mueller and Y. Huang, *Science*, 2015, **348**, 1230–1234.
18 D. Guo, R. Shibuya, C. Akiba, S. Saji, T. Kondo and J. Nakamura, *Science*, 2016, **351**, 361–365.
19 W. Xia, A. Mahmood, Z. Liang, R. Zou and S. Guo, *Angew. Chem., Int. Ed.*, 2016, **55**, 2650–2676.
20 Y. J. Sa, C. Park, H. Y. Jeong, S.-H. Park, Z. Lee, K. T. Kim, G.-G. Park and S. H. Joo, *Angew. Chem., Int. Ed.*, 2014, **53**, 4102–4106.
21 Y. Jia, L. Zhang, A. Du, G. Gao, J. Chen, X. Yan, C. L. Brown and X. Yao, *Adv. Mater.*, 2016, **28**, 9532–9538.
22 Y. Liang, H. Wang, J. Zhou, Y. Li, J. Wang, T. Regier and H. Dai, *J. Am. Chem. Soc.*, 2012, **134**, 3517–3523.
23 Y. Liang, Y. Li, H. Wang, J. Zhou, J. Wang, T. Regier and H. Dai, *Nat. Mater.*, 2011, **10**, 780–786.
24 Z.-S. Wu, S. Yang, Y. Sun, K. Parvez, X. Feng and K. Müllen, *J. Am. Chem. Soc.*, 2012, **134**, 9082–9085.
25 H. Zhu, S. Zhang, Y.-X. Huang, L. Wu and S. Sun, *Nano Lett.*, 2013, **13**, 2947–2951.
26 S. Mao, Z. Wen, T. Huang, Y. Hou and J. Chen, *Energy Environ. Sci.*, 2014, **7**, 609–616.

27 C. Li, X. Han, F. Cheng, Y. Hu, C. Chen and J. Chen, *Nat. Commun.*, 2015, **6**, 7345.
28 Q.-L. Zhu, W. Xia, T. Akita, R. Zou and Q. Xu, *Adv. Mater.*, 2016, **28**, 6391–6398.
29 Y. Zhu, B. Zhang, X. Liu, D.-W. Wang and D. S. Su, *Angew. Chem., Int. Ed.*, 2014, **53**, 10673–10677.
30 Y.-Z. Chen, C. Wang, Z.-Y. Wu, Y. Xiong, Q. Xu, S.-H. Yu and H.-L. Jiang, *Adv. Mater.*, 2015, **27**, 5010–5016.
31 S. Zhao, H. Yin, L. Du, L. He, K. Zhao, L. Chang, G. Yin, H. Zhao, S. Liu and Z. Tang, *ACS Nano*, 2014, **8**, 12660–12668.
32 G. Wu, K. L. More, C. M. Johnston and P. Zelenay, *Science*, 2011, **332**, 443–447.
33 K. Gong, F. Du, Z. Xia, M. Durstock and L. Dai, *Science*, 2009, **323**, 760–764.
34 L. Zhang and Z. Xia, *J. Phys. Chem. C*, 2011, **115**, 11170–11176.
35 Z. Yang, Z. Yao, G. Li, G. Fang, H. Nie, Z. Liu, X. Zhou, X. Chen and S. Huang, *ACS Nano*, 2012, **6**, 205–211.
36 J. Zhang and L. Dai, *ACS Catal.*, 2015, **5**, 7244–7253.
37 W. Zhang, Z.-Y. Wu, H.-L. Jiang and S.-H. Yu, *J. Am. Chem. Soc.*, 2014, **136**, 14385–14388.
38 W. Niu, L. Li, X. Liu, N. Wang, J. Liu, W. Zhou, Z. Tang and S. Chen, *J. Am. Chem. Soc.*, 2015, **137**, 5555–5562.
39 J. Y. Cheon, J. H. Kim, J. H. Kim, K. C. Goddeti, J. Y. Park and S. H. Joo, *J. Am. Chem. Soc.*, 2014, **136**, 8875–8878.
40 Z. Xu, X. Zhuang, C. Yang, J. Cao, Z. Yao, Y. Tang, J. Jiang, D. Wu and X. Feng, *Adv. Mater.*, 2016, **28**, 1981–1987.
41 G. Wang, Y. Sun, D. Li, H.-W. Liang, R. Dong, X. Feng and K. Müllen, *Angew. Chem., Int. Ed.*, 2015, **54**, 15191–15196.
42 H.-W. Liang, X. Zhuang, S. Brüller, X. Feng and K. Müllen, *Nat. Commun.*, 2014, **5**, 4973.
43 J. Sun, H. Yin, P. Liu, Y. Wang, X. Yao, Z. Tang and H. Zhao, *Chem. Sci.*, 2016, **7**, 5640–5646.
44 Y. Zheng, Y. Jiao, M. Jaroniec, Y. Jin and S. Z. Qiao, *Small*, 2012, **8**, 3550–3566.
45 L. Lai, J. R. Potts, D. Zhan, L. Wang, C. K. Poh, C. Tang, H. Gong, Z. Shen, J. Lin and R. S. Ruoff, *Energy Environ. Sci.*, 2012, **5**, 7936–7942.
46 C. Zhang, R. Hao, H. Liao and Y. Hou, *Nano Energy*, 2013, **2**, 88–97.
47 T. Xing, Y. Zheng, L. H. Li, B. C. C. Cowie, D. Gunzelmann, S. Z. Qiao, S. Huang and Y. Chen, *ACS Nano*, 2014, **8**, 6856–6862.
48 Z. Zhao, M. Li, L. Zhang, L. Dai and Z. Xia, *Adv. Mater.*, 2015, **27**, 6834–6840.
49 Y. Jiao, Y. Zheng, M. Jaroniec and S. Z. Qiao, *J. Am. Chem. Soc.*, 2014, **136**, 4394–4403.
50 H.-X. Zhong, J. Wang, Y.-W. Zhang, W.-L. Xu, W. Xing, D. Xu, Y.-F. Zhang and X.-B. Zhang, *Angew. Chem., Int. Ed.*, 2014, **53**, 14235–14239.
51 E. M. Miner, T. Fukushima, D. Sheberla, L. Sun, Y. Surendranath and M. Dincă, *Nat. Commun.*, 2016, **7**, 10942.
52 S. Chen, J. Bi, Y. Zhao, L. Yang, C. Zhang, Y. Ma, Q. Wu, X. Wang and Z. Hu, *Adv. Mater.*, 2012, **24**, 5593–5597.
53 H.-W. Liang, W. Wei, Z.-S. Wu, X. Feng and K. Müllen, *J. Am. Chem. Soc.*, 2013, **135**, 16002–16005.
54 L. Hao, S. Zhang, R. Liu, J. Ning, G. Zhang and L. Zhi, *Adv. Mater.*, 2015, **27**, 3190–3195.
55 Y.-C. Lin, P.-Y. Teng, C.-H. Yeh, M. Koshino, P.-W. Chiu and K. Suenaga, *Nano Lett.*, 2015, **15**, 7408–7413.
56 P. Kuhn, A. Forget, D. Su, A. Thomas and M. Antonietti, *J. Am. Chem. Soc.*, 2008, **130**, 13333–13337.
57 P. Kuhn, M. Antonietti and A. Thomas, *Angew. Chem., Int. Ed.*, 2008, **47**, 3450–3453.
58 S. Ren, M. J. Bojdys, R. Dawson, A. Laybourn, Y. Z. Khimyak, D. J. Adams and A. I. Cooper, *Adv. Mater.*, 2012, **24**, 2357–2361.
59 C. E. Chan-Thaw, A. Villa, P. Katekomol, D. Su, A. Thomas and L. Prati, *Nano Lett.*, 2010, **10**, 537–541.
60 X. Feng, X. Ding and D. Jiang, *Chem. Soc. Rev.*, 2012, **41**, 6010–6022.
61 K. Iwase, T. Yoshioka, S. Nakanishi, K. Hashimoto and K. Kamiya, *Angew. Chem., Int. Ed.*, 2015, **54**, 11068–11072.
62 S. Hug, L. Stegbauer, H. Oh, M. Hirscher and B. V. Lotsch, *Chem. Mater.*, 2015, **27**, 8001–8010.
63 X. Zhu, C. Tian, S. M. Mahurin, S.-H. Chai, C. Wang, S. Brown, G. M. Veith, H. Luo, H. Liu and S. Dai, *J. Am. Chem. Soc.*, 2012, **134**, 10478–10484.
64 L. Hao, J. Ning, B. Luo, B. Wang, Y. Zhang, Z. Tang, J. Yang, A. Thomas and L. Zhi, *J. Am. Chem. Soc.*, 2015, **137**, 219–225.
65 K. Kamiya, R. Kamai, K. Hashimoto and S. Nakanishi, *Nat. Commun.*, 2014, **5**, 5040.
66 X. Long, J. Li, S. Xiao, K. Yan, Z. Wang, H. Chen and S. Yang, *Angew. Chem., Int. Ed.*, 2014, **53**, 7584–7588.
67 Y. Hou, Z. Wen, S. Cui, S. Ci, S. Mao and J. Chen, *Adv. Funct. Mater.*, 2015, **25**, 872–882.
68 L. Jiao, Y.-X. Zhou and H.-L. Jiang, *Chem. Sci.*, 2016, **7**, 1690–1695.
69 Y. Su, Y. Liu, P. Liu, D. Wu, X. Zhuang, F. Zhang and X. Feng, *Angew. Chem., Int. Ed.*, 2015, **54**, 1812–1816.
70 L. Qie, W.-M. Chen, Z.-H. Wang, Q.-G. Shao, X. Li, L.-X. Yuan, X.-L. Hu, W.-X. Zhang and Y.-H. Huang, *Adv. Mater.*, 2012, **24**, 2047–2050.
71 S. Zhang, P. Kang, S. Ubnoske, M. K. Brennaman, N. Song, R. L. House, J. T. Glass and T. J. Meyer, *J. Am. Chem. Soc.*, 2014, **136**, 7845–7848.
72 M. Park, J. Ryu, Y. Kim and J. Cho, *Energy Environ. Sci.*, 2014, **7**, 3727–3735.
73 J. Masa, W. Xia, I. Sinev, A. Zhao, Z. Sun, S. Grützke, P. Weide, M. Muhler and W. Schuhmann, *Angew. Chem., Int. Ed.*, 2014, **53**, 8508–8512.
74 S. C. Ray, Z. N. Tetana, R. Erasmus, W.-F. Pong and N. J. Coville, *Appl. Phys. A*, 2014, **115**, 153–157.
75 J. Tang, J. Liu, C. Li, Y. Li, M. O. Tade, S. Dai and Y. Yamauchi, *Angew. Chem., Int. Ed.*, 2015, **54**, 588–593.
76 D. Deng, X. Pan, L. Yu, Y. Cui, Y. Jiang, J. Qi, W.-X. Li, Q. Fu, X. Ma, Q. Xue, G. Sun and X. Bao, *Chem. Mater.*, 2011, **23**, 1188–1193.
77 P. Wang, Z. Wang, L. Jia and Z. Xiao, *Phys. Chem. Chem. Phys.*, 2009, **11**, 2730–2740.
78 K. Qiu, G. Chai, C. Jiang, M. Ling, J. Tang and Z. Guo, *ACS Catal.*, 2016, **6**, 3558–3568.

79 Y. Zheng, Y. Jiao, J. Chen, J. Liu, J. Liang, A. Du, W. Zhang, Z. Zhu, S. C. Smith, M. Jaroniec, G. Q. Lu and S. Z. Qiao, *J. Am. Chem. Soc.*, 2011, **133**, 20116–20119.
80 S. Yang, X. Feng, X. Wang and K. Müllen, *Angew. Chem., Int. Ed.*, 2011, **50**, 5339–5343.
81 W. Yang, T.-P. Fellinger and M. Antonietti, *J. Am. Chem. Soc.*, 2011, **133**, 206–209.
82 F. Pan, J. Jin, X. Fu, Q. Liu and J. Zhang, *ACS Appl. Mater. Interfaces*, 2013, **5**, 11108–11114.
83 Y. Zhan, J. Huang, Z. Lin, X. Yu, D. Zeng, X. Zhang, F. Xie, W. Zhang, J. Chen and H. Meng, *Carbon*, 2015, **95**, 930–939.
84 J. Wu, C. Jin, Z. Yang, J. Tian and R. Yang, *Carbon*, 2015, **82**, 562–571.
85 J. Zhang, L. Qu, G. Shi, J. Liu, J. Chen and L. Dai, *Angew. Chem., Int. Ed.*, 2016, **55**, 2230–2234.
86 J. Yang, H. Sun, H. Liang, H. Ji, L. Song, C. Gao and H. Xu, *Adv. Mater.*, 2016, **28**, 4606–4613.
87 H. Yu, L. Shang, T. Bian, R. Shi, G. I. N. Waterhouse, Y. Zhao, C. Zhou, L.-Z. Wu, C.-H. Tung and T. Zhang, *Adv. Mater.*, 2016, **28**, 5080–5086.
88 R. Gokhale, S. M. Unni, D. Puthusseri, S. Kurungot and S. Ogale, *Phys. Chem. Chem. Phys.*, 2014, **16**, 4251–4259.
89 X. Zhou, Z. Yang, H. Nie, Z. Yao, L. Zhang and S. Huang, *J. Power Sources*, 2011, **196**, 9970–9974.
90 D. Yu, Y. Xue and L. Dai, *J. Phys. Chem. Lett.*, 2012, **3**, 2863–2870.
91 P. Zhang, F. Sun, Z. Xiang, Z. Shen, J. Yun and D. Cao, *Energy Environ. Sci.*, 2014, **7**, 442–450.
92 C. Han, J. Wang, Y. Gong, X. Xu, H. Li and Y. Wang, *J. Mater. Chem. A*, 2014, **2**, 605–609.
93 L. Ye, G. Chai and Z. Wen, *Adv. Funct. Mater.*, 2017, **27**, 1606190.
94 X. Wang, J. S. Lee, Q. Zhu, J. Liu, Y. Wang and S. Dai, *Chem. Mater.*, 2010, **22**, 2178–2180.

